

Fault locking near Istanbul: indication of earthquake potential from InSAR and GPS observations

Faqi Diao,^{1,2} Thomas R. Walter,¹ Giuseppe Solaro,³ Rongjiang Wang,¹
 Manuela Bonano,³ Mariarosaria Manzo,³ Semih Ergintav,⁴ Yong Zheng,²
 Xiong Xiong² and Riccardo Lanari³

¹GFZ German Research Center for Geosciences, Telegrafenberg, D-14473 Potsdam, Germany. E-mail: faqidiao@whigg.ac.cn

²State Key Laboratory of Geodesy and Earth's Dynamics, Institute of Geodesy and Geophysics, Chinese Academy of Sciences, Wuhan 430077, China

³Istituto per il Rilevamento Elettromagnetico dell' Ambiente (IREA), Consiglio Nazionale delle Ricerche (CNR), Via Diocleziano 328, I-80124 Napoli, Italy

⁴Department of Geodesy, Kandilli Observatory and Earthquake Research Institute, Boğaziçi University, 34680 Istanbul, Turkey

Accepted 2016 January 27. Received 2016 January 27; in original form 2015 October 24

SUMMARY

A sequence of large earthquakes occurred along the North Anatolian fault in the 20th century. These earthquakes, including the 1999 İzmit/Düzce earthquakes, generally propagated westward towards the Marmara Sea, defining the Main Marmara fault as a potential seismic gap. It is important to conduct a detailed assessment of the seismic hazards along the main Marmara fault because the megacity Istanbul lies only approximately 10 km north of the eastern segment of the Main Marmara fault, which is referred to as the Princes' Islands Fault segment (PIF). Here, we study the locking status of this fault segment to evaluate the seismic hazard potential. For the first time, combined ascending and descending Interferometric Synthetic Aperture Radar and Global Positioning System observations were used to investigate the crustal deformation associated with the PIF. After careful corrections of the estimated ground velocity, a deformation pattern relating to fault locking near the Princes' Islands was identified. The modeling results revealed that the slip rate and locking depth of the fault segment show a clear trade-off, which were estimated as $18.9 \pm 7.2 \text{ mm yr}^{-1}$ and $12.1 \pm 7.0 \text{ km}$, respectively. With a moment accumulation rate of $1.7 \pm 0.4 \times 10^{17} \text{ Nm yr}^{-1}$ (proportional to the product of slip rate and locking depth), our results imply a build-up of a geodetic moment on the PIF and therefore a potential for earthquake hazards in the vicinity of the Istanbul megacity.

Key words: Satellite geodesy; Seismic cycle; Continental tectonics: strike-slip and transform.

1 INTRODUCTION

Before the occurrence of earthquakes, faults are loaded by tectonic stresses, which may be affected by other geological activities (such as the post-seismic effect and nearby volcano eruption). Fault segments may experience different states during a seismic cycle: co- and post-seismic slip, aseismic creep or interseismic locking (Bürgmann *et al.* 2000; Moreno *et al.* 2010; Schurr *et al.* 2014), which change the loading condition along faults and associated hazards. The status of a fault is routinely recorded by geodetic and seismic techniques, which allow for estimations of the location and magnitude of the fault slip, creep or slip deficit (Bürgmann *et al.* 2000; Moreno *et al.* 2010). These parameters are essential for the assessment of potential earthquake hazards (e.g. Schurr *et al.* 2014).

The North Anatolian Fault Zone (NAFZ) is one of the most active faults worldwide, extending approximately 1200 km from eastern Turkey to the northern Aegean Sea (Şengör *et al.* 2004). Along the fault, the Anatolian Plate moves westward relative to the Eurasian

Plate at a rate of approximately 24 mm yr^{-1} (Reilinger *et al.* 2006). During the 20th century, a series of damaging earthquakes occurred along the NAFZ, which generally propagated westward towards Istanbul, a city with more than 14 million inhabitants (Fig. 1). The latest event in this series of earthquakes occurred in 1999, approximately 80 km east of Istanbul. No large earthquake has occurred on the Princes' Islands fault (PIF) since 1776 (Pondard *et al.* 2007). Therefore, the PIF, located just offshore of Istanbul, is considered to be a slip-deficient segment (e.g. Parsons 2004; Bohnhoff *et al.* 2013; Ergintav *et al.* 2014). Previous studies have indicated that the stress on the PIF has been enhanced by stable tectonic loading and adjacent earthquake activity, resulting in high earthquake potential in the near future (e.g. Parsons 2004).

Assessing the locking status of a seismogenic fault is essential for evaluating future seismic hazards at the same fault or at adjacent fault segments (e.g. Bürgmann *et al.* 2000). At the PIF south of Istanbul, two end-member hypotheses may result in different hazard assessments. If this fault segment has been completely locked since

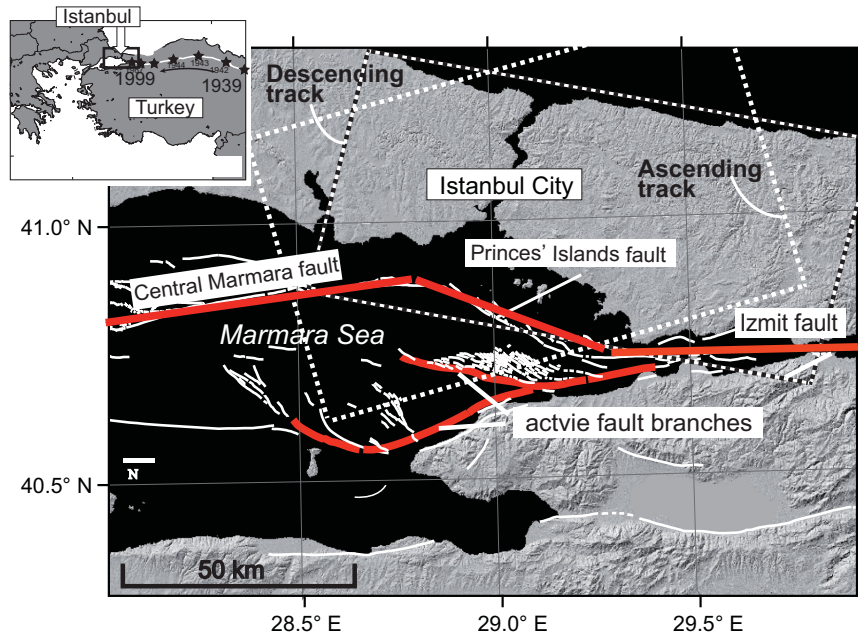


Figure 1. Tectonic setting of the research area. Solid red lines show the main fault segments and branches in this area, whereas the white lines indicate the distribution of small faults (Armijo *et al.* 2005). Black stars in the upper left-hand panel represent large earthquakes ($M > 7$) that occurred during the last century along the North Anatolian Fault.

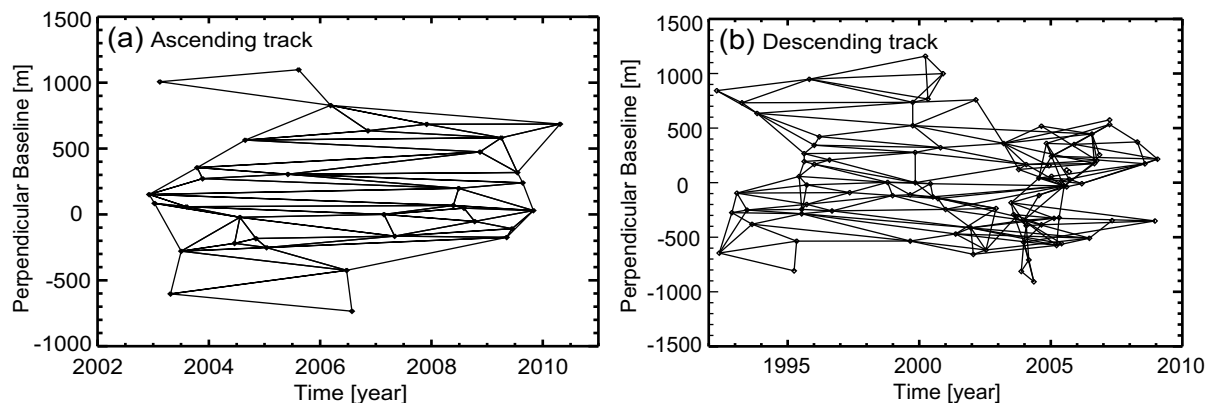


Figure 2. Temporal and perpendicular baselines for the interferograms used in this study on the ascending track (Envisat) and descending track (ERS). The dots denote SAR acquisitions, whereas the lines indicate the interferometric pairs used to generate the time-series.

the last large event in 1776, a large slip deficit would have been built-up (Hergert & Heidbach 2010; Bohnhoff *et al.* 2013). In contrast, if the fault is not completely locked or is subject to creep, the total accumulated strain may be smaller. Thus, the fault-locking status is critical for assessing the current potential of seismic hazards near the PIF.

Crustal deformation in the vicinity of the PIF can be recorded by geodetic techniques and provide direct evidence relating to fault locking and the slip rate. Ergintav *et al.* (2014) analysed Global Positioning System (GPS) observations and inferred that the PIF is locked with a slip rate of $10\text{--}15\text{ mm yr}^{-1}$. The few GPS sites available, however, do not permit a locking depth analysis of the fault segment, although additional observation sites could potentially provide stronger constraint of strain accumulation on the fault segment. In this paper, we investigate the fault-locking status at the PIF segment by using Interferometric Synthetic Aperture Radar (InSAR) and GPS observations. Because deformation signals are influenced by other processes, such as the post-seismic viscoelas-

tic relaxation of the adjacent 1999 İzmit/Düzce earthquakes, we performed model-based signal decomposition and then studied the decomposed data to determine the fault-locking status near Istanbul.

2 InSAR AND GPS DATA

To investigate the crustal deformation near Istanbul, we processed satellite images acquired from the ERS and ENVISAT European Space Agency satellites from both ascending (2002–2009) and descending (1992–2009) orbits (Fig. 2). Starting with these data, 323 interferograms were produced by exploiting the well-developed Small Baseline Subsets (SBAS) method (Berardino *et al.* 2002). The interferogram generation was carried out by exploiting a 90-m Shuttle Radar Topography Mission Digital Elevation Model (DEM) of the study area and precise orbital information. Moreover, a complex multilook operation with 4 range looks and 20 azimuth looks was performed, resulting in a pixel size of approximately $100 \times 100\text{ m}$. The SBAS method

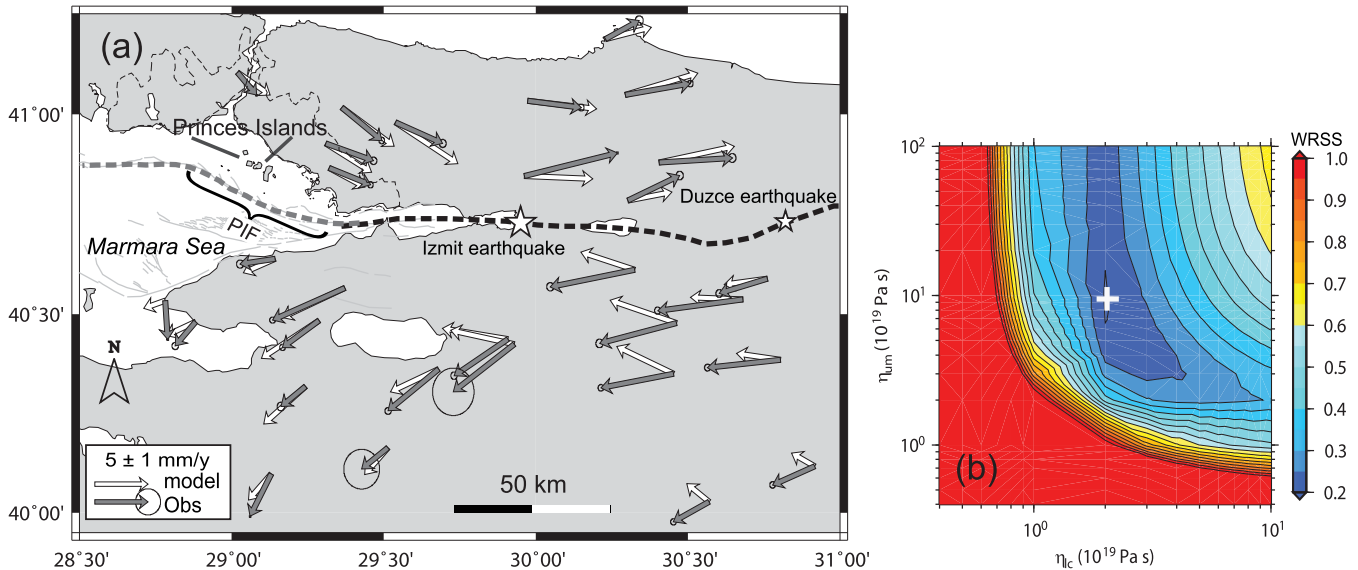


Figure 3. (a) Post-seismic GPS velocities observed between 2002 and 2009 (grey arrows with 95 per cent confidence error ellipses). White arrows represent the predictions of the optimal viscoelastic model (with lower crust and upper-mantle viscosities of 2.0×10^{19} Pa s and 9.0×10^{19} Pa s, respectively). The dashed black line marks the surface rupture of the İzmit/Düzce earthquakes and the white stars on the dashed black lines mark the epicentre of the İzmit and Düzce events. The thick, dashed grey line shows the location of the eastern main Marmara fault. The thin dashed grey line shows the boundary of Istanbul. (b) Misfit variations in searching for the optimal viscosities of the lower crust (η_{lc}) and upper mantle (η_{um}) using post-seismic GPS velocities.

allowed us to retrieve mean displacement velocity maps and corresponding time-series with a standard deviation of approximately 1 mm yr^{-1} , in agreement with previous studies (Casu *et al.* 2006; Bonano *et al.* 2013).

The key steps of the SBAS approach are the following:

(1) The data pairs used to generate the multilook DInSAR interferograms are chosen to mitigate the decorrelation phenomena (Zebker & Villasenor 1992). In particular, this data pair selection involves the introduction of constraints on the allowed maximum spatial and temporal separation (baseline) between the orbits relevant to the interferometric SAR image pairs, thus maximizing the number of coherent pixels in the generated interferograms. In this paper, we imposed a maximum perpendicular baseline value of approximately 400 m.

(2) The phase unwrapping operation of the original (wrapped) phase from the modulo- 2π restricted (wrapped) signal is directly carried out from the generated multilook interferograms by exploiting the extended minimum cost flow procedure (Pepe & Lanari 2006).

(3) The singular value decomposition (SVD) method is applied to ‘combine’ the unwrapped DInSAR interferograms by searching for a least-squares solution with a minimum norm energy constraint to compute the deformation time-series on a (coherent) pixel-by-pixel basis (Berardino *et al.* 2002).

(4) In the presence of possible orbital fringes caused by inaccuracies in the SAR sensors orbit information, our approach allows the estimation of these orbital patterns by searching for the best-fit ramp to the temporal high-pass/spatially low-pass time-series signal component; following this step, we remove the detected ramps from each differential interferograms (Pepe *et al.* 2011).

(5) As a final step, a space–time filtering operation is carried out to estimate and remove possible artefacts due to atmospheric inhomogeneities between the acquisition pairs. This operation is based on the observation that the atmospheric signal phase component is highly correlated in space but poorly in time. Accordingly, the undesired atmospheric phase signal is estimated from the time-series

computed via the SVD technique through the cascade of a low-pass filtering step in the 2-D spatial domain followed by a temporal high-pass filtering operation.

We finally estimated the mean crustal velocity of both ascending and descending tracks for the period from 2002 to 2009. This time period was selected because it allows detailed comparisons of ascending InSAR data to descending InSAR data and InSAR data to GPS data from GPS sites near Princes’ Islands, which were established after 2002 (Ergintav *et al.* 2009). This period also provides the best ERS and Envisat data acquisition and density. The InSAR data provide more than 80 000 coherent pixels in both ascending and descending tracks. To allow for further modeling, we resampled the original data using the simple uniform downsampling method as presented in Pritchard *et al.* (2002), which can retain the details from a smooth deformation signal as were desired for the PIF segment.

The GPS observation data between 2002 and 2009 were processed to obtain the crustal velocity using GAMIT/GLOBK software following the strategy of Ergintav *et al.* (2009). The stable interseismic component was removed based on the estimated velocity field from pre-seismic GPS observations (Wang *et al.* 2009). The GPS data therefore provide a valuable data set for estimating the post-seismic deformation process after the 1999 İzmit/Düzce earthquakes (Fig. 3a).

3 SIGNAL DECOMPOSITION

As the research area is located at the vicinity of the 1999 İzmit/Düzce earthquakes, the crustal deformation observed between 2002 and 2009 (Fig. 4) may include the post-seismic relaxation effect of the İzmit/Düzce earthquakes (e.g. Ergintav *et al.* 2009; Wang *et al.* 2009). Moreover, due to the limited spatial coverage of the observations, we focus on the PIF; however, the crustal deformation may be influenced by the locking/creep of adjacent faults (i.e. the İzmit fault in the east, the main Marmara fault in the west and other

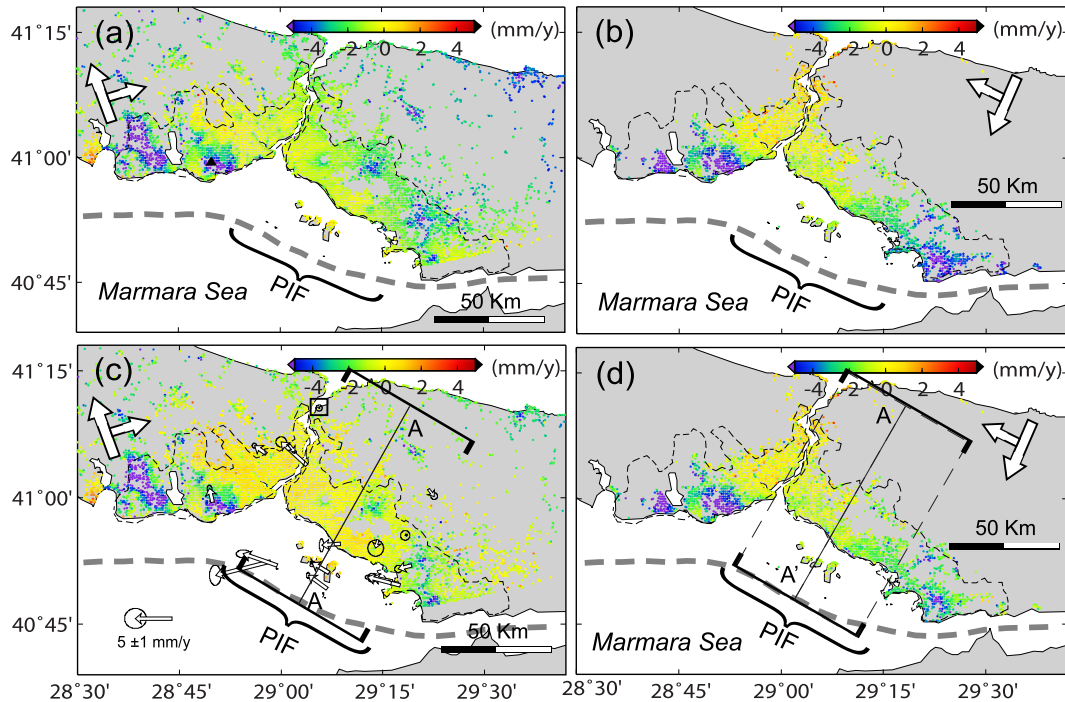


Figure 4. The InSAR velocities in the line-of-sight direction along the PIF. (a) and (b) are original InSAR velocities observed between 2002 and 2009; (c) and (d) are InSAR velocities after removing the effects of viscoelastic relaxation and adjacent faults. Positive values indicate pixels that are moving towards the satellite. The thin, dashed grey line shows the boundary of Istanbul. A–A' represents the location of velocity profile shown in Figs 5 and 6. Arrows in (c) show GPS velocities with 95 per cent confidence error ellipses inferred from Ergintav *et al.* (2014). The black square is the reference point of the GPS.

fault branches near the PIF; Fig. 1). In addition, a number of local effects caused by soil compaction and landslides (e.g. Akarvardar *et al.* 2009; Walter *et al.* 2010) may affect our data at small scales (Fig. 4). A pronounced subsidence area that is located to the west of Istanbul lies outside of the velocity profile used for our modeling analysis and did not affect our modeling results.

Our modeling and analysis strategy thus accounts for overlapped deformation signals. First, the post-seismic viscoelastic relaxation effect (PVRE) was investigated based on GPS data observed between 2002 and 2009. Then, the effect of adjacent faults was estimated based on models inferred from previous studies (Hergert & Heidbach 2010; Ergintav *et al.* 2014). The two effects were removed from the observations as described in the following sections before inverting the locking status and slip rate of the PIF.

3.1 Post-seismic viscoelastic relaxation effect caused by the 1999 earthquakes

The relaxation process of the viscoelastic lower crust and/or upper mantle that is driven by the coseismic stress changes may continue for decades and plays an important role in crustal deformation following large earthquakes (Bürgmann & Dresen 2008). GPS observations spanning the same period as the InSAR data were used to estimate the viscoelastic relaxation effect during this period that was induced by the 1999 İzmit/Düzce earthquakes (Fig. 3a).

A three-layer viscoelastic model was established to simulate the post-seismic GPS velocities by employing the PSGRN/PSCMP code (Wang *et al.* 2006). The model includes one elastic upper-crust layer and two viscoelastic layers representing the lower crust and upper mantle; the Maxwell rheology was applied to both latter layers (Fig. S1). The Crustal 2.0 model (Mooney *et al.* 1998) was used to obtain the physical parameters in each layer (Fig. S1).

The thickness of the elastic upper crust was fixed to 20 km; this value was inferred from the depth distribution of the regional seismicity (Karabulut *et al.* 2011). A coseismic slip model that drives viscoelastic relaxation was adopted from Wright *et al.* (2001). The viscosities of the Maxwell rheology remained to be solved in the viscoelastic relaxation model.

A grid search method was used to approach the optimal Maxwell viscosities of the lower crust (η_{lc}) and the upper mantle (η_{um}), which were found to be 2.0×10^{19} Pa s and 9.0×10^{19} Pa s, respectively (Fig. 3b). The optimal viscosities can explain the observations of most stations to the first order, although clear misfit was observed for stations that are southeast of the İzmit rupture. A similar phenomenon was observed by Hearn *et al.* (2009) and may be related to some unknown local tectonic background. We then calculated the PVRE at each InSAR data point using the derived optimal parameters and then removed it to obtain InSAR velocities that are largely free of post-seismic effect. The calculated PVRE is significant (Fig. 5a), indicating that the post-seismic viscoelastic relaxation plays an important role in controlling the surface deformation in this area after the 1999 İzmit/Düzce earthquake.

In addition, we found that the lower crust viscosity (η_{lc}) could be well solved, but the upper-mantle viscosity (η_{um}) was subject to larger uncertainty (with a lower bound of 4.0×10^{19} Pa s). Therefore, in a parametric study, the PVRE was calculated using different η_{um} values to determine how the calculated PVRE depends on the variation in η_{um} . The analysis revealed that the PVRE (in line-of-sight direction, LOS) of ascending InSAR data changes only slightly for different η_{um} values applied (Fig. S2). The descending InSAR data, in turn, show a clear dependence on η_{um} due to the LOS geometric effect (Fig. S2). To evaluate how such data-based bias on η_{um} would affect the final inversion results, additional tests were performed and the results are discussed in Section 5.2.

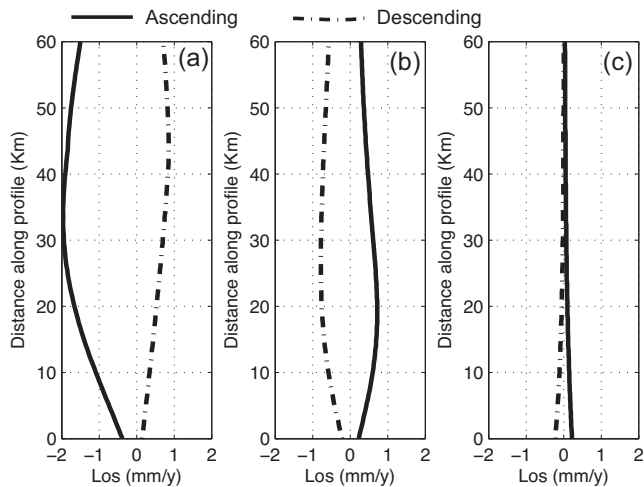


Figure 5. Deformation along the profile induced by (a) post-seismic viscoelastic relaxation of the 1999 İzmit/Düzce earthquakes, (b) the effect of the İzmit fault and central Marmara faults and (c) the locking of fault branches south of the PIF (Fig. 1) on the velocity profile shown in Fig. 4.

3.2 Effect of adjacent faults

We investigated the locking status of the PIF using the local crustal deformation data; however, the deformation may be affected by the locking of fault segments at the two sides of the PIF (i.e. the İzmit fault segment on the eastern side and the central Marmara fault on the western side). Therefore, we designed a simple dislocation model to estimate the effect induced by locking or creep of the two adjacent fault segments. Uniform slip accumulation rates derived by Ergintav *et al.* (2014) were assigned to the fault segments on either side of the PIF (25 mm yr^{-1} for the İzmit segment and 2 mm yr^{-1} for

the west central segment). Note that we used the slip accumulation rate here as the faults almost has no effect on deformation north of the PIF if they are subject to complete creep. Based on our modeling, the deformation induced by these adjacent faults was calculated and removed from each InSAR data point. As the results show, the effect was found to be smaller compared with that induced by post-seismic viscoelastic relaxation (Fig. 5).

Hergert & Heidbach (2010) indicated that fault branches located near the main Marmara fault may play a secondary role in the total slip rate. Here, we estimated the contribution of such fault branches south of the PIF (Fig. 1) assuming that these fault branches are locked with slip rates as inferred by Hergert & Heidbach (2010) and a locking depth of 15 km. The estimated results for the ascending and descending tracks are shown in Fig. 5(c), and both are less than 0.2 mm yr^{-1} , which is markedly less than the effect of the viscoelastic relaxation and below the geodetic detection threshold. We inferred that the observed deformations result mainly from the slip along the PIF, as detailed in the following sections.

4 SLIP RATE AND LOCKING DEPTH OF THE PIF

After removing the effects of post-seismic viscoelastic relaxation and the effect of adjacent faults, both the ascending and descending InSAR velocity fields near the Princes' Islands show a deformation pattern relating to fault movement at the PIF (Figs 4 and 6). A velocity profile (in the LOS direction) excluding the subsidence area southwest of Istanbul (Akarvardar *et al.* 2009) was constructed from the residual InSAR deformation (Figs 4 and 6) and used to estimate the fault slip rate and locking depth by employing a 2-D screw dislocation model (Savage & Burford 1973). We assumed that all deformation is fault parallel and horizontal and that the

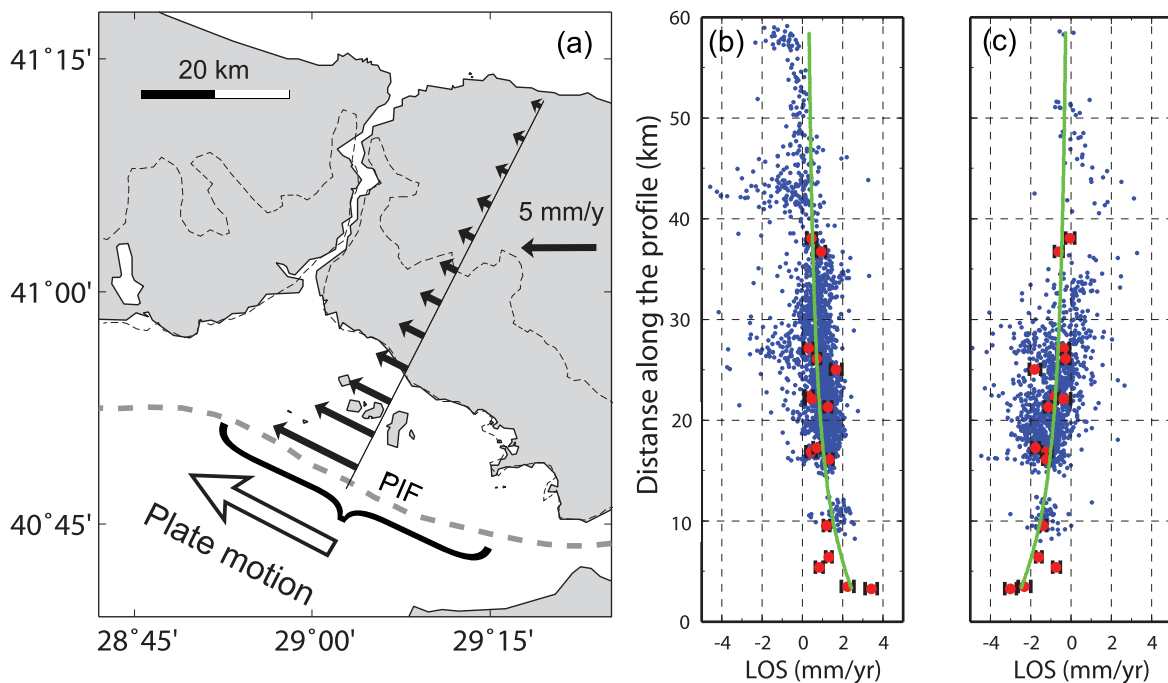


Figure 6. Velocity profiles perpendicular to the PIF. (a) Modeled horizontal velocities along the profile derived from the optimal parameters (slip rate: 18.9 mm yr^{-1} ; locking depth: 12.1 km). The reference point of the velocity is located at the vanishing point of the profile. (b) and (c) show the ascending and descending InSAR data. Red dots represent GPS velocities along the profile (error bars show $1-\sigma$ uncertainties of the velocities), which were projected onto LOS directions. The green curves show forward-modeled velocity profiles using optimal slip rate and locking depth. The thin, dashed grey line shows the boundary of Istanbul.

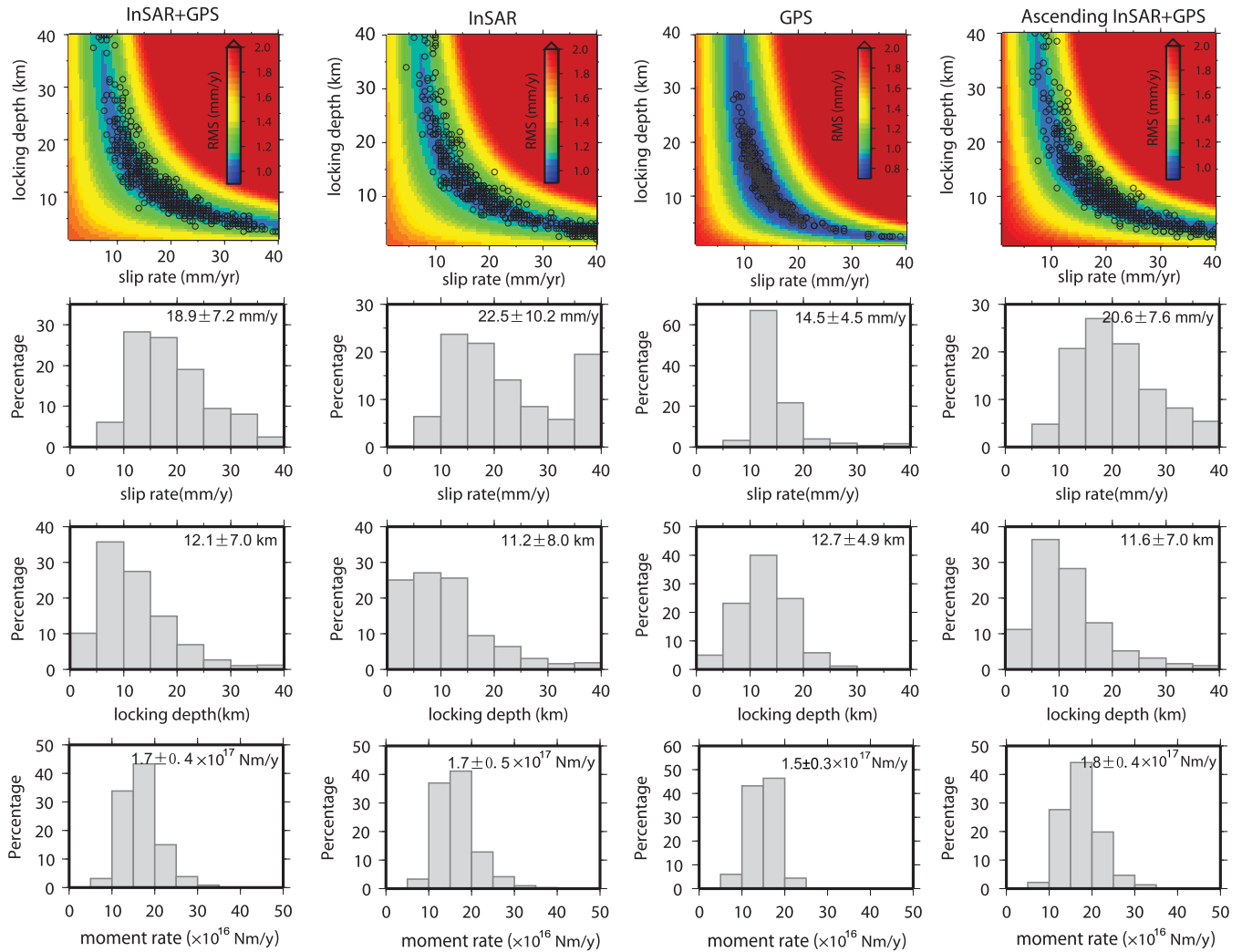


Figure 7. Dextral slip rates versus fault locking depth inferred from LOS velocity profile of different data sets. Figures in each column represent results that were inferred from different data sets. The colour in the first row indicates the misfit calculated from each combination of slip rate and locking depth. The black circles shape the distribution of the optimal parameters based on the Monte Carlo analysis. Figures in the lower rows reveal the statistical distribution of slip rate, locking depth and moment accumulation rate.

velocity (v) as a function of its perpendicular distance to the fault (x) can be represented by $v(x) = (V)/\pi \times \arctan(x/D)$, where V and D are the slip rate and the locking depth, respectively. We carried out a parameter search for slip rate and locking depth over ranges of $1\text{--}40\text{ mm yr}^{-1}$ and $1\text{--}40\text{ km}$ with 0.5 mm yr^{-1} and 0.5 km intervals, respectively. We calculated the rms (root mean square) misfit between the model and data set for each combination of the parameters and then obtained the optimal values that minimize the rms misfit.

First, we performed a joint inversion by combing the ascending InSAR data, descending InSAR data and GPS data together. Second, we analysed the different data separately, wherein models were constructed considering the InSAR data only or the GPS data only. In the combined inversion, we used the Helmert variance component estimation method to calculate the relative weight ratios of each data set (Xu *et al.* 2010). According to this method, the relative weight of each data set is determined based on the posterior misfit information of the data set. By using an iterative process (Xu *et al.* 2010), the relative weight ratios between ascending InSAR data, descending InSAR data and GPS data were converged to 0.474, 0.154 and 0.372, respectively, and were not affected by the initial weight ratios

that were assigned. The GPS data used in the slip rate estimation are described in Ergintav *et al.* (2014), for which the post-seismic deformation has been estimated and removed. The effect driven by adjacent faults that were included in the GPS data was also removed using the method mentioned above (in Section 3.2).

A Monte Carlo method was applied to statistically estimate the uncertainty of the obtained optimal parameters (e.g. Walters *et al.* 2011). We first constructed the variance–covariance matrix using the method of Biggs *et al.* (2007) and generated spatially correlated noise. Then, we added the noise to the observations to obtain the perturbed data set. Finally, we performed the parameter search using the disturbed data set and obtained the best-fitting model. These steps were conducted 500 times to estimate the uncertainty of the parameters.

The distribution of the slip rate and locking depth that were inferred from the Monte Carlo simulation (the second and third rows of Fig. 7) shows general consistency with the rms misfit map. The statistical result reveals a slip rate of $18.9 \pm 7.2\text{ mm yr}^{-1}$ and a locking depth of $12.1 \pm 7.0\text{ km}$ (the mean value \pm the $1\text{-}\sigma$ uncertainty) based on the joint InSAR and GPS data (Fig. 7). Investigation using only the InSAR data yielded a similar result (second column) but

with relatively larger uncertainty. Compared with the InSAR data, the GPS data indicate a similar slip rate ($14.5 \pm 4.5 \text{ mm yr}^{-1}$). Although the InSAR data are noisier than the GPS data, the data density of the InSAR observation is almost 100 times larger than the GPS data, which may improve the robustness of the inversion result in some extent. The small uncertainty of the GPS result is mainly due to the high observation precision ($\sim 0.5 \text{ mm yr}^{-1}$). However, statistical inspection of the results revealed clear trade-offs between slip rate and the locking depth, revealing the limitation of the data coverage in solving the two parameters. The observations can be generally explained well with slip rates ranging between 8 and 40 mm yr^{-1} combined with decreased locking depths ranging from 40 to 3 km, with important implications further discussed below.

Our inversion results indicate that the PIF is possibly highly locked (large locking depth) with small slip rates or partly locked (shallow locking depths) with high slip rates. By assuming a uniform length (30 km) of the PIF and a shear modulus (30 GPa) of the crust, we calculated the moment accumulation rate of this fault segment based on the obtained locking depth and slip rate; the statistical distribution is shown in Fig. 7 (fourth row). Although both slip rate and locking depth are subject to large uncertainty, the derived moment accumulation rate appears to converge to similar values close to $1.7 \pm 0.4 \times 10^{17} \text{ Nm yr}^{-1}$ when using different data.

5 DISCUSSION

In this paper, InSAR and GPS observations were analysed to explore the fault-locking status at the PIF segment, 10 km south of Istanbul. After removing the effects that were caused by viscoelastic relaxation and locking/creep of adjacent faults, we found clear strain accumulation at the eastern main Marmara fault in the vicinity of the Princes' Islands. Analysing the combined InSAR and GPS data, the optimal slip rate on the fault was estimated at $18.9 \pm 7.2 \text{ mm yr}^{-1}$ combined with a locking depth of $12.1 \pm 7.0 \text{ km}$. Clear trade-offs between the two parameters were observed resulting from poor data coverage close to the submarine fault. Therefore, this study emphasizes the need for geodetic observation close to the fault to more precisely estimate the degree of locking. However, the uncertainties of the results are large due to the limited data coverage. The uncertainties of the slip rate and locking depth inferred by Monte Carlo simulation suggests that the PIF may be highly locked or subject to partial creep with a locking depth ranging from 19 to 5 km (with a 68 per cent confidence level, Fig. 7). We believe that the use of InSAR data and GPS data is limited for assessing the slip rate and locking depth of this region. Therefore, improved data coverage, such as the use of submarine borehole geodetic observations, is highly necessary for further assessing the earthquake potential of this fault segment.

5.1 Limitations

We performed 2-D screw dislocation modeling to describe the fault status of the PIF although assessing the slip deficit distribution along the PIF may improve the estimation of the seismic hazard near Istanbul. The reasons for employing the simple model are (1) sample data were only available for the north side of the fault, which may be insufficient for a distributed slip deficit inversion in this case; and (2) the 2-D model based on the velocity profile could avoid the effect of local deformation southwest of Istanbul city.

In addition, this study relied on geodetic data to infer fault-locking status at a fault segment hidden beneath the sea, involving

additional limitations. First, the InSAR and GPS observations were limited to the north side of the fault due to the fault's geographical position, subjecting the inverted slip rate and locking depth to large variation. However, the general consistency in deformation pattern between the InSAR and GPS data give us confidence that the observed signal accurately reflects the locking status of the PIF. Second, some local effects such as landslide and subsidence may affect the small-scale deformation pattern; however, the largest local effect is located southwest of Istanbul and did not change the large-scale deformation pattern of the velocity profile used in our inversion. Third, we used a three-layer model to account for the viscoelastic effect, and some secondary contributions (such viscosity inhomogeneity) were neglected. Finally, the geodetic data covered only the last 10 yr; therefore, our results have no temporal resolution and cannot address the history of the fault slip rate and locking status.

5.2 Uncertainty induced by signal decomposition

To investigate the crustal movement associated with the fault slip rate and locking status, two effects, comprising the effects of the PVRE and adjacent faults, were estimated and removed from the observed InSAR data. However, the modeling of these two effects may have affected the results as described below.

First, the long-term PVRE was estimated and removed from the observed InSAR deformation. However, we found that η_{um} was subject to large uncertainty although obtained value of this parameter agrees well with previous investigations (e.g. Wang *et al.* 2009). Further investigations with more data (such as more GPS data and gravity data) are required to improve the robustness of this parameter. Additional simulation using different values of η_{um} indicated that variation in η_{um} only affected the predicted PVRE (in the LOS direction) of the descending track (Fig. S2). To avoid the effect induced by the uncertainty in η_{um} , the slip rate and locking depth were estimated by using the ascending InSAR data and GPS data only. As shown in Fig. 7, the results are similar to those inferred from the joint inversion of all of the InSAR and GPS data. This similarity led us to conclude that the large uncertainty in η_{um} did not significantly affect the final results. It should be mentioned that additional inversions by omitting the descending tract data were only sensitivity tests. In fact, we still regard the inversion result inferred from all InSAR data and GPS data as the final result of this paper. Furthermore, we consider that a proper approach would be to regard the inversion as a four-parameter problem (two viscosities, locking depth and slip rate), and search the optimal values of the four parameters. However, we consider that the InSAR data almost have no resolution on the viscosities in the post-seismic viscoelastic model.

Second, we calculated the effect of adjacent faults based on previous kinematic studies (Hergert & Heidbach 2010; Ergintav *et al.* 2014). Due to geometric and tectonic fault complexity, possible trade-offs between the slip rate of the PIF and that of the adjacent faults may occur. However, seismic and geomechanical results support the hypothesis that the main PIF plays a dominant role in this area (Hergert & Heidbach 2010; Bohnhoff *et al.* 2013).

5.3 Data coverage problem revealed by synthetic tests

Two inversion tests were carried out to investigate how the uncertainty of the inverted slip rate and locking depth depend on the data coverage. We first generated synthetic data based on the screw

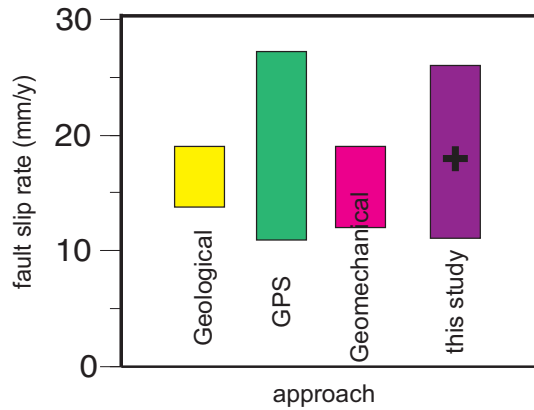


Figure 8. Comparison of fault slip rates obtained using different approaches. The geological results shown are from Armijo *et al.* (1999) and Gasperini *et al.* (2011). The GPS results are from Reilinger *et al.* (2006) and Ergintav *et al.* (2014), in which fault-locking depth was fixed in their inversions. The geomechanical result is from Hergert & Heidbach (2010).

dislocation model with known input parameters (red lines in upper panels of Fig. S3). The data were then disturbed by adding noise. The disturbed data were regarded as the ‘observations’ used for the synthetic tests. Second, we performed a parameter search and Monte Carlo simulation to obtain the optimal estimation and the uncertainty of the parameters using the same method as described in Section 4.

Not unexpectedly, the uncertainty of the inversion results indicated a high dependency on data coverage (Fig. S3); that is, poor data coverage corresponded to large uncertainty. However, we found that the solved optimal slip rate and locking depth were close to the input values. Moreover, the moment accumulation rate could be obtained with similar precision as that inferred from the data with a hypothetical perfect coverage (Fig. S3). Therefore, we conclude that the results and interpretation presented here regarding the locking conditions of the PIF are justifiable.

5.4 Comparisons with previous results and implications

As shown in Fig. 8, the derived slip rate in this paper agrees with the average level of slip rates obtained by previous geodetic studies (Reilinger *et al.* 2006; Ergintav *et al.* 2014). Slip rates estimated from finite-element modeling (Hergert & Heidbach 2010) or geological study (Armijo *et al.* 1999; Gasperini *et al.* 2011) are slightly low. However, these differences between geodetic and geological results are subtle and can be partially explained by the effect of surrounding secondary faults (Hergert & Heidbach 2010). Furthermore, we assumed a pure strike-slip motion in estimating the slip rate, and the extension of the fault was neglected in our study (i.e. a normal slip component), which may play a minor role (Ergintav *et al.* 2014). The PIF segment is possibly more complexly arranged with varying dip and strike and also accommodates some dip-slip movement, which we did not further elaborate here due to data limitation.

Microseismic observations between 2006 and 2010 in the PIF zone indicated an inactive patch at 0–10 km depth with a length of approximately 30 km in the vicinity of the Princes’ Islands (Bohnhoff *et al.* 2013). The derived fault locking depth (12.1 ± 7.0 km) determined from our models agrees well with this seismic result. In addition, the inverted moment accumulation rate remained stable and had relatively small uncertainty compared with the inverted slip

rate and locking depth. By assuming a uniform moment accumulation rate since the last rupture in 1776 (Pondard *et al.* 2007), the total accumulated seismic moment on this segment ($4.1 \pm 1.0 \times 10^{19}$ Nm yr⁻¹) is sufficient for the generation of an earthquake with $M \approx 7$, assuming the PIF segment to be 30 km long.

6 CONCLUSIONS

The analysis of a large geodetic data set at the PIF segment revealed a superposition of different deformation phenomena. A model-based signal decomposition approach allowed us to study the degree of fault locking of this potentially hazardous seismogenic fault near Istanbul. The slip rate was estimated as 18.9 ± 7.2 mm yr⁻¹ with an estimated locking depth of 12.1 ± 7.0 km. However, large uncertainties exist in these parameters that result from poor data coverage close to the fault, highlighting the need for geodetic monitoring system much closer to the fault that are presently available. Successful hazard assessment and early warning largely depends on greater near-fault data availability.

ACKNOWLEDGEMENTS

The InSAR data used in this paper were provided by the European Space Agency. This work was supported by the MARSite project funded by the European Union (grant no. 308417), the National Natural Science Foundation of China (grant nos 41304017 and 41274104), the visiting scholar programme of the Chinese Academy of Science (grant no. 2012–128) and the HGF Helmholtz Alliance EDA. This work was also partially supported by the I-AMICA project (PONA3_00363) financed under the National Operational Programme (NOP) for ‘Research and Competitiveness 2007–2013’ cofunded with the European Regional Development Fund (ERDF) and National Resources. We thank UNAVCO for technical support for the continuous and survey GPS observations. We thank the editor Duncan Agnew, David Mencin and an anonymous reviewer for their constructive comments.

REFERENCES

- Akarvardar, S., Feigl, K.L. & Ergintav, S., 2009. Ground deformation in an area later damaged by an earthquake: monitoring the Avclar district of Istanbul, Turkey, by satellite radar interferometry, *Geophys. J. Int.*, **178**, 976–988.
- Armijo, R., Meyer, B., Hubert, A. & Barka, A., 1999. Westward propagation of the North Anatolian fault into the northern Aegean: timing and kinematics, *Geology*, **27**, 267–270.
- Armijo, R. *et al.*, 2005. Submarine fault scarps in the Sea of Marmara pull-apart (North Anatolian Fault): implications for seismic hazard in Istanbul, *Geochem. Geophys. Geosyst.*, **6**, Q06009, doi:10.1029/2004GC000896.
- Berardino, P., Fornaro, G., Lanari, R. & Sansosti, E., 2002. A new algorithm for surface deformation monitoring based on small baseline differential SAR interferograms, *IEEE Trans. Geosci. Remote Sens.*, **40**, 2375–2383.
- Biggs, J., Wright, T., Lu, Z. & Parsons, B., 2007. Multi-interferogram method for measuring interseismic deformation: Denali Fault, Alaska, *Geophys. J. Int.*, **170**, 1165–1179.
- Bohnhoff, M., Fatih, B., Georg, D., Malin, P.E., Eken, T. & Aktar, M., 2013. An earthquake gap south of Istanbul, *Nat. Commun.*, **4**, 1999, doi:10.1038/ncomms2999.
- Bonano, M., Manunta, M., Pepe, A., Paglia, L. & Lanari, R., 2013. From previous C-band to new X-band SAR systems: assessment of the DInSAR mapping improvement for deformation time-series retrieval in urban areas, *IEEE Trans. Geosci. Remote Sens.*, **51**, 1973–1984.

- Bürgmann, R. & Dresen, G., 2008. Rheology of the lower crust and upper mantle: evidence from rock mechanics, geodesy, and field observations, *Ann. Rev. Earth planet. Sci.*, **36**, 531–567.
- Bürgmann, R., Schmidt, D., Nadeau, R.M., d’Alessio, M., Fielding, E., Manaker, D., McEvilly, T.V. & Murray, M.H., 2000. Earthquake potential along the northern Hayward fault, California, *Science*, **289**, 1178–1182.
- Casu, F., Manzo, M. & Lanari, R., 2006. A quantitative assessment of the SBAS algorithm performance for surface deformation retrieval from DInSAR data, *Remote Sens. Environ.*, **102**(3), 195–210.
- Ergintav, S. et al., 2009. Seven years of postseismic deformation following the 1999, $M = 7.4$ and $M = 7.2$, Izmit-Düzce, Turkey earthquake sequence, *J. geophys. Res.*, **114**, B07403, doi:10.1029/2008JB00602.
- Ergintav, S. et al., 2014. Istanbul’s earthquake hot spots: geodetic constraints on strain accumulation along faults in the Marmara seismic gap, *Geophys. Res. Lett.*, **41**, 5783–5788.
- Gasperini, L., Polonia, A., Çağatay, M.N., Bortoluzzi, G. & Gerrante, V., 2011. Geological slip rates along the North Anatolian Fault in the Marmara region, *Tectonics*, **30**, TC6001, doi:10.1029/2011TC002906.
- Hergert, T. & Heidbach, O., 2010. Slip-rate variability and distributed deformation in the Marmara Sea fault system, *Nat. Geosci.*, **3**, 132–135.
- Hearn, E.H., McClusky, S., Ergintav, S. & Reilinger, R.E. 2009. Izmit earthquake postseismic deformation and dynamics of the North Anatolian Fault Zone, *J. geophys. Res.*, **114**, B08405, doi:10.1029/2008JB006026.
- Karabulut, H. et al., 2011. Evolution of the seismicity in the eastern Marmara Sea a decade before and after the 17 August 1999 Izmit earthquake, *Tectonophysics*, **510**, 17–27.
- Mooney, W.D., Laske, G. & Masters, T.G., 1998. CRUST 5.1: a global crustal model at $5^\circ \times 5^\circ$, *J. geophys. Res.*, **103**, 727–747.
- Moreno, M., Rosenau, M. & Oncken, O., 2010. Maule earthquake slip correlates with pre-seismic locking of Andean subduction zone, *Nature*, **467**, 198–202.
- Parsons, T., 2004. Recalculated probability of Mw 7 earthquakes beneath the Sea of Marmara, Turkey, *J. geophys. Res.*, **109**, B05304, doi:10.1029/2003JB002667.
- Pepe, A. & Lanari, R., 2006. On the extension of the minimum cost flow algorithm for phase unwrapping of multi-temporal differential SAR interferograms, *IEEE Geosci. Remote Sens. Lett.*, **44**, 2374–2383.
- Pepe, A., Berardino, P., Bonano, M., Euillades, L.D., Lanari, R. & Sansosti, E., 2011. SBAS-based satellite orbit correction for the generation of DInSAR time-series: application to RADARSAT-1 data, *IEEE Trans. Geosci. Remote Sens.*, **49**, 5150–5165.
- Pondard, N., Armijo, R., King, G.C.P., Meyer, B. & Flerit, F., 2007. Fault interactions in the Sea of Marmara pull-apart (North Anatolian Fault): earthquake clustering and propagating earthquake sequences, *Geophys. J. Int.*, **171**(3), 1185–1197.
- Pritchard, M.E., Simons, M., Rosen, P.A., Hensley, S. & Webb, F.H., 2002. Co-seismic slip from the 1995 July 30 $M_w = 8.1$ Antofagasta, Chile, earthquake as constrained by InSAR and GPS observations, *Geophys. J. Int.*, **150**, 362–376.
- Reilinger, R.E. et al., 2006. GPS constraints on continental deformation in the Africa-Arabia-Eurasia continental collision zone and implications for the dynamics of plate interactions, *J. geophys. Res.*, **111**, V05411, doi:10.1029/2005JB004051.
- Savage, J.C. & Burford, R.O., 1973. Geodetic determination of relative plate motion in central California, *J. geophys. Res.*, **78**, 832–845.
- Schurr, B. et al., 2014. Gradual unlocking of plate boundary controlled initiation of the 2014 Iquique earthquake, *Nature*, **512**, 299–302.
- Şengör, A.M.C., Tuysuz, O., Imren, C., Sakiñ, M., Eyidoğa, H., Görür, N., Le Pichon, X. & Rangin, C., 2004. The North Anatolian fault: a new look, *Ann. Rev. Earth planet. Sci.*, **33**, 1–75.
- Walter, T.R. et al., 2010. Geohazard supersite: InSAR monitoring at Istanbul city, *EOS, Trans. Am. geophys. Un.*, **91**, 313–324.
- Wang, R., Lorenzo-Martín, F. & Roth, F., 2006. PSGRN/PSCMP—a new code for calculating co- and post-seismic deformation, geoid and gravity changes based on the viscoelastic-gravitational dislocation theory, *Comput. Geosci.*, **32**, 527–541.
- Wang, L., Wang, R., Roth, F., Enescu, B., Hainzl, S. & Ergintav, S., 2009. Afterslip and viscoelastic relaxation following the 1999 M7.4 Izmit earthquake from GPS measurements, *Geophys. J. Int.*, **178**, 1220–1237.
- Wright, T., Fielding, E. & Parsons, B., 2001. Triggered slip: observations of the 17 August 1999 Izmit (Turkey) earthquake using radar interferometry, *Geophys. Res. Lett.*, **28**, 1079–1082.
- Walters, R.J., Holley, R.J., Parsons, B. & Wright, T.J., 2011. Inter-seismic strain accumulation across the North Anatolian Fault from Envisat InSAR measurements, *Geophys. Res. Lett.*, **38**, L05303, doi:10.1029/2010GL046443.
- Xu, C., Liu, Y., Wen, Y. & Wang, R., 2010. Coseismic slip distribution of the 2008 Mw 7.9 Wenchuan earthquake from joint inversion of GPS and InSAR data, *Bull. seism. Soc. Am.*, **100**(5B), 2736–2749.
- Zebker, H.A. & Villasenor, J., 1992. Decorrelation in interferometric radar echoes, *IEEE Trans. Geosci. Remote Sens.*, **30**, 950–959.

SUPPORTING INFORMATION

Additional Supporting Information may be found in the online version of this paper:

Figure S1. Layered earth model of the research area used in this study: the left-hand panel shows seismic velocity and the right-hand panel shows density.

Figure S2. Deformation along the profile induced by the post-seismic viscoelastic relaxation effect with different values of upper-mantle viscosity.

Figure S3. Results of synthetic tests with different levels of data coverage. The left-hand side of the figure shows the simulated data (upper panel) and the results of Test 1, in which only data from one side of the fault were used. The right-hand side of the figure is similar to that of the left-hand side, but data from both sides of the fault were used. The symbols are as described in Fig. 7.

(<http://gji.oxfordjournals.org/lookup/suppl/doi:10.1093/gji/ggw048/-/DC1>).

Please note: Oxford University Press is not responsible for the content or functionality of any supporting materials supplied by the authors. Any queries (other than missing material) should be directed to the corresponding author for the paper.